Applied Materials Today 29 (2022) 101627

Contents lists available at ScienceDirect

Applied Materials Today

journal homepage: www.elsevier.com/locate/apmt

Electrochemical pumping: An alternative solution for hydrogen embrittlement

Jinwoo Kim [a,1], Xiahui Yao [b,1], Decheng Kong [a], Ju Li [a,b,*], Bilge Yildiz [a,b,*], C. Cem Tasan [a,*]

[a] Department of Materials Science and Engineering, Massachusetts Institute of Technology, 77 Massachusetts Avenue, Cambridge, MA 02139, United States
[b] Department of Nuclear Science and Engineering, Massachusetts Institute of Technology, 77 Massachusetts Avenue, Cambridge, MA 02139, United States

ARTICLE INFO

Keywords:
Hydrogen
Steels
Healing
Electrochemistry
Damage
Desorption

ABSTRACT

Hydrogen embrittlement is a form of chemo-mechanical damage that is special in that it can be partially reversible. Here, we propose a method for recovering structural alloys from hydrogen embrittlement at room temperature by electrochemically biased desorption of hydrogen. We demonstrate that the method can enable the reversion of hydrogen-induced degradation of mechanical properties, by comparing the mechanical behavior of commercial stainless steel specimens at different hydrogen charging and desorption states. These case studies also reveal the influence of electrochemical potential, H content and the characteristics of H trapping sites, on the effectiveness of this recovery approach. The limitations arising from the presence of unhealable forms of hydrogen damage, and the generic applicability of this electrochemically-assisted recovery method are also discussed.

Regulating hydrogen (H) inventory is fundamental for preventing H embrittlement (HE) in structural metals. The transport processes that result in H uptake and, in-turn, embrittlement effects, can be classified into three steps: (i) H ingress through the material surfaces, (ii) H diffusion and trapping inside the material, and (iii) H desorption. In order to block the first step, H-ingress, introducing physical H barriers such as oxide or nitride layers with low H-permeability is a typical solution [1,2]. The low mechanical reliability of these brittle H barriers, however, introduces a limit to their applicability, especially for ambient temperature applications [1]. Utilizing chemical inhibitors could be another method to reduce H ingress into metals, in applications where the hydrogen gas purity is not a critical factor [1]. Once H diffuses in, it generally degrades ductility and fracture toughness, through various interactions with crystallographic defects [3,4]. HE solutions associated with this second step are based on alloy and microstructure design to introduce reversible or irreversible H traps [2,5]. Such design solutions, in favorable microstructures, can even trigger beneficial effects of H uptake, such as solid-solution strengthening or mechanical twinning [6–8]. Extensive efforts to prevent HE have been made focusing on these two steps, aiming to regulate H ingress and internal interactions as briefly described above. Despite the great progress made, H-induced failures are still a major concern for a large number of industrial applications [9,10].

Regulating H desorption, the third step, has received relatively less attention due to associated practical difficulties. It is widely known that thermally-induced desorption can be an effective strategy to remove hydrogen from even the deepest microstructural traps [11,12]. In fact, this is the basis of thermal desorption spectroscopy, which is widely used to measure the H content in a specimen [13]. Yet, several practical challenges associated with heat treatments (e.g. surface oxidation, temperature control, unwanted phase transformations) render this strategy difficult to apply in engineering practice. In this study, we propose a new method for preventing steels from hydrogen embrittlement at room temperature (RT), which relies on electrochemically biased desorption of H: electrochemical H pumping. We confirmed that the method can effectively help several commercial steels to recover from the H-induced mechanical degradation, by comparing the tensile deformation behavior of H pre-charged specimens after uncontrolled desorption in air and electrochemically controlled desorption experiments.

To demonstrate this method, we tested commercial AISI 430 ferritic stainless steel (430SS) and AISI 420 martensitic stainless steel (420SS),

* Corresponding authors at: Department of Materials Science and Engineering, Massachusetts Institute of Technology, 77 Massachusetts Avenue, Cambridge, MA 02139, United States.
E-mail addresses: liju@mit.edu (J. Li), byildiz@mit.edu (B. Yildiz), tasan@mit.edu (C.C. Tasan).
[1] These authors contributed equally to this work.

https://doi.org/10.1016/j.apmt.2022.101627
Received 19 January 2022; Received in revised form 31 July 2022; Accepted 16 August 2022

which meet ASTM A240, to verify the accelerated recovery from HE by electrochemical pumping. The compositions of the steel specimens provided by their manufacturer are shown in Table 1. The thickness of the steel sheets was 0.3 mm. We measured the effective diffusion coefficient (D_{eff}) of the two stainless steels by the electrochemical H-permeation method using a Devanathan-Stachurski H-permeation cell, according to ASTM G148-97. The steel sheets were cut to tensile test specimens (gauge area of 7.5 mm × 5 mm for 430SS, 7.5 mm × 3 mm for 420SS, respectively) using wire electrical discharge machining, before H pre-charging. Electrochemical processes for H pre-charging, Pd electrodeposition and H-removal were performed in a simple three-electrode cell described in Fig. S1 in Supplementary Materials. H pre-charging was conducted electrochemically in the galvanostatic mode, using an aqueous solution of 5 vol% H_2SO_4 and 3 g/L NH_4SCN and a platinum (Pt) wire as the electrolyte and counter electrode, respectively. For electrochemical H removal, a 0.1 M NaOH solution and a Pt wire were used as the electrolyte and counter electrode, respectively. Palladium (Pd) particles were deposited on the specimen surface between the H pre-charging and removal process, using a solution of 5 g/L $PdCl_2$ in 30 vol% $NH_3{\bullet}H_2O$ and a constant current density of 1.5 mA/cm^2. All steps of the electrochemical treatments and property measurements were performed promptly right after the previous, in order to minimize H loss between the steps. The processes of H-charging, Pd-coating and H-removal were conducted within an interval of 15 s (i.e., for quick cleaning of specimens and Pt electrodes with deionized water, and blowing). Tensile tests were conducted within 60 s after the electrochemical treatments, using a Deben MTEST2000 mechanical testing system with the maximum strain rate of the machine (8.89×10^{-4}/s) to minimize H desorption during the tensile test. The strain values of data points in stress-strain curves are recalculated by digital image correlation (DIC) using speckle ink patterns on the sample surface. The amount of total H in specimens was measured by the inert gas fusion method using a Horiba EMGA-830 ONH analyzer, calibrated with standard steel specimens with 2.3 ± 0.4, 4.5 ± 0.4, 6.0 ± 0.5 wppm, respectively. The measurements were also performed promptly within 60 s after the electrochemical treatments. The Pd layer on the specimens was removed before H content measurements by fine polishing using a P4000 SiC paper, since the Pd layer can absorb hydrogen desorbed from the specimens. No thickness reduction after the Pd removal procedure was detected by a micrometer with a resolution of 1 μm. The measurements were conducted repeatedly with three specimens for each electrochemical treatment condition. The microstructures and fracture surfaces of the specimens were observed using a TESCAN MIRA3 scanning electron microscope (SEM) and a TESCAN AMBER X SEM equipped with an Oxford Instruments Symmetry 3 electron back-scattered diffraction (EBSD) detector.

The electrochemical cell configuration for H-removal is described in Fig. 1(a).[2] The cell configuration is analogous to the half-cell of the oxidation side in the Devanathan-Stachurski H-permeation cell [14]. A metallic material that is subject to prevention of or recovery from HE works as the anode, and H near the interface between the material and the electrolyte is continuously oxidized to protons (H^+) in the electrolyte and removed from the material. This creates a large concentration gradient of H between the inner volume and the surface region of the material, which accelerates the H diffusion in the material toward the surface and the continuous H removal. The mechanism will be discussed in detail later with experimental results. The electrode potential should be selected in the range where it is high enough to oxidize atomic H to solvated proton while it does not induce severe corrosion of the metal. From a cyclic voltammogram of the Pd coated 430SS in Fig. 1(b), the redox peaks corresponding to the H reduction and oxidation on Pd particles were found at approximately −0.75 to −0.25 V versus Hg/HgO electrode in 0.1 M NaOH solution, and the potential for H removal from the steel could be selected in the plateau region above the redox peaks. We tested the H oxidation potential of +0.3 V and +0.6 V versus Hg/HgO reference electrode in the potentiostatic mode in this work.

Pd nanoparticles are introduced on the metal surface as an electrocatalyst to promote the H oxidation reaction. Fig. 1(c) presents the effectiveness of Pd particles on H removal, by comparing H-oxidation current density change by time between a bare steel specimen and a Pd-coated steel specimen, both pre-charged with H in the same condition. The coated specimen shows a higher oxidation current at the initial stage compared to the bare specimen, which indicates faster H removal from the specimen by Pd. Because the total H content is the same in both cases, the H oxidation current in the Pd-coated specimen becomes lower than that of the bare specimen after the large H removal in a short time at the initial stage.

We first tested the electrochemically biased recovery of HE in the 430SS that has a high H diffusivity at RT and is susceptible to HE [15]. The 430SS sheet has a microstructure of equiaxed ferrite grains, as shown in Fig. 2(a). The grain size of the 430SS is 10.7 μm (estimated from the area-weighted mean of the equivalent circle diameter of the grains in the EBSD scan). The measured value of effective H-diffusion coefficient (D_{eff}) for the 430SS specimen is 1.92×10^{-12} m^{2}s^{-1} (See Supplementary Materials for the H-permeation test result). H was pre-charged in the 430SS specimens using a current density (i_c) of 0.5 mA cm^{-2} for 20 min. The diffusion distance (L) estimated by the equation [16], $L = 2\sqrt{Dt}$ (where the factor of 2 is applied due to H ingress from two surfaces), is ~96 μm. Although the H diffusion distance is shorter than the specimen thickness (300 μm), the specimen exhibits a clear reduction of fracture strain (ε_f) and hardening behavior after H-charging, as shown in Fig. 2(b). The fracture strain of uncharged (H-free) and H-charged specimens are 30.22 ± 0.65% and 18.32 ± 0.58%, respectively (averaged from 4 specimens for each case). The embrittlement behavior after H charging is also evidenced by the transition of fracture surface morphology from ductile fracture with dimples (Fig. 3(a,e)) to quasi-cleavage fracture (Fig. 3(b,f)). The quasi-cleavage fracture morphology prevailing throughout the whole fracture surface of the H-charged specimen indicates that the H-charging condition is severe enough to diffuse H and cause embrittlement throughout the specimen thickness.

Due to its high H diffusivity at RT, the specimen can partially recover from HE by H desorption in the ambient condition (i.e. when the specimen is left at room temperature in the air, without electrochemistry[3]) for 12 h (Fig. 2(b)). But even after another 12 h, the uncontrolled desorption does not recover the specimen further. Moreover, the fracture surface of the specimen after 24 h-desorption exhibits a mixed mode of dimples and quasi-cleavage fracture in a random spatial distribution, as shown in Fig. 3(c,g). These can be attributed to the remaining H trapped at defects such as grain boundaries and dislocations [2,17–19], rather than diffusing towards the free surface even after extended H desorption. On the other hand, the electrochemically biased H removal can recover the mechanical properties of the H-charged specimen to its pristine state (within the error range) in 300 min using the H oxidation potential (V_p) of 0.3 V (vs. Hg/HgO reference electrode), as shown in Fig. 2(c). The fracture surface of the specimen (Fig. 3(d)) also returns to a dimple-dominant morphology and shows a similar reduction of area with the uncharged case. The recovery can be accelerated by increasing the potential within the range where severe corrosion does not occur. At the initial stage of electrochemically-stimulated recovery (~20 min), the

[2] The schematic diagram in Fig. 1(a) only shows an enlarged view between the two electrodes. The actual cell used in this work is a simple three-electrode cell configuration and is described in Fig. S1 in Supplementary Materials.

[3] It should be noted that those specimens left in the air for the uncontrolled desorption does not have any electrodeposited Pd layer, in contrast to the specimens subjected to the electrochemically stimulated desorption. The Pd layer has only negligible effect on H-desorption without electrochemical stimulation. See Fig. S2 in Supplementary for details.

Table 1
Alloy compositions of AISI 430SS and 420SS tested in this work.

Elements [wt.%]	Fe	C	Cr	Mn	Mo	P	Si	S	V
430SS	79.30–83.93	0–0.12	16–18	0–1	0–0.5	0.04	0–1	0.03	–
420SS	82.17–87.15	0.15–0.46	12–14	0.4–1	0–1	0–0.04	0–1	0–0.03	0.3

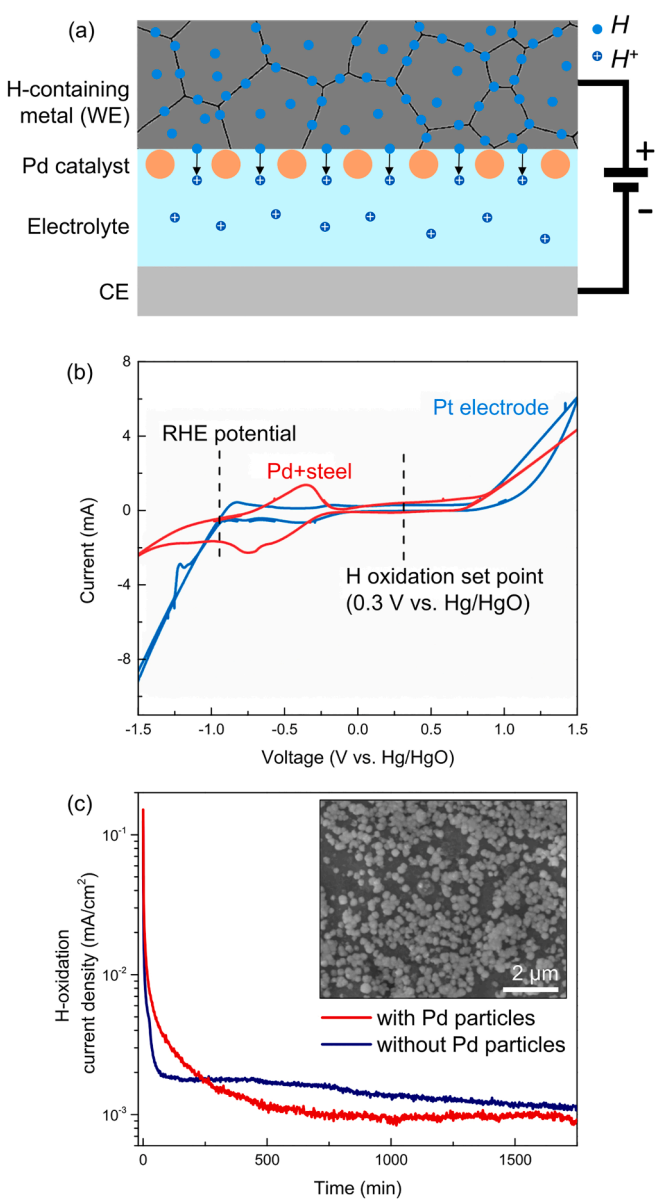

Fig. 1. (a) Schematic diagram of the electrochemical H-pumping cell. (b) Determination of H oxidation potential in a cyclic voltammogram. (c) H-oxidation curves from the H pre-charged 420SS specimen surfaces with and without Pd catalyst particles. The inset image shows the electrodeposited Pd particles on the steel surface.

case with V_p = 0.6 V (Fig. 2(d)) exhibits approximately three times larger recovery than that with V_p = 0.3 V (Fig. 2(c)), in terms of the fraction of fracture strain recovery ($\equiv(\varepsilon_f - \varepsilon_{f,H})/(\varepsilon_{f,0} - \varepsilon_{f,H})$, where $\varepsilon_{f,0}$ *and* $\varepsilon_{f,H}$ are the fracture strain of uncharged and H-charged specimens, respectively). The complete recovery to the original state is able to be achieved in 90 min with the higher oxidation potential of V_p = 0.6 V. The fraction of recovery from HE in this material depending on recovery methods and time is summarized in Fig. 2(e).

Residual hydrogen contents in the 430SS sheets were also measured before and after H-desorption (Fig. 2(f)). The uncharged 430SS has 2.53 ± 0.65 weight ppm (wppm) of H, and H-charging in the tested condition loads approximately 5.75 wppm of H into the specimen (total 8.28 ± 0.74 wppm H). H-desorption in ambient air conditions for 24 h removes around half of the charged H, reducing the H content to 5.54 ± 0.42 wppm. On the other hand, the electrochemically biased recovery with V_p = 0.6 V for 20 min reduces the H content in the steel to 5.34 ± 0.55 wppm, which is close to that in the specimen after 24 h-desorption in the air. This result corresponds well with the fracture strain recovery shown in Fig. 2(e). The electrochemically stimulated recovery for 90 min reduces the H content further to 3.64 ± 0.20 wppm. Given that the tensile specimens recovered in the same electrochemical condition exhibit comparable ductility with the uncharged specimen, ~1 wppm residue of charged H might be lower than a threshold level of H causing embrittlement. The results prove that the electrochemical method significantly promotes H desorption from the material and is able to fully recover from HE quickly, which is difficult by the uncontrolled desorption into the air in the short time scale.

An intriguing point of this electrochemically assisted H-removal is that oxidizing atomic H just at the surface effectively stimulates the accelerated desorption of H. The electrical current does not directly carry or move the internal H. The anodic potential applied to the specimen oxidizes H only at the material surface, which are either solute H in the first atomic layer at the surface or chemisorbed H atoms that can far exceed the amount of solute H at the surface (the physisorbed H_2 molecules can be disregarded here due to their weak bonding to the surface [20]). The comparison result between desorption in the ambient air condition and in the electrochemically-assisted condition in Fig. 2 reveals that the surface H impedes the removal of internal H. The chemisorbed hydrogen atoms must recombine to H_2 molecules before leaving the surface in the ambient air and the recombination rate depends on the distance between H atoms, or H coverage at the surface [20]. The adsorption energy of chemisorbed H on metal surface ranges from around 50 to 150 kJ/mol [20], which is similar to or higher than H-binding energy at strong trapping sites in microstructure [2]. In other words, the surface H is difficult to be removed by natural desorption in the ambient air at RT. On the other hand, the electrochemical oxidation of surface H to H^+can effectively remove the surface-abundant H and accelerates the egress of internal H towards the material surface, which is proved by the results in Fig. 2.

We also tested the effectiveness of electrochemically-stimulated HE recovery in a high-strength martensitic stainless steel, 420SS, as high-strength steels with tensile strengths above 950 MPa are generally susceptible to HE [21]. The 420SS has a lower value of effective H-diffusion coefficient (D_{eff} = 7.94 × 10^{-13} m^2 s^{-1}) than the ferritic 430SS. The microstructure of the 420SS tested in this work is shown in Fig. 4(a). The material consists of fine martensite laths and carbide precipitates under 1 μm (the elliptical phase in a dark contrast in the BSE image), including a high density of H-trapping sites such as martensite block/packet boundaries,[4] prior austenite grain boundary, carbide-matrix interface, as well as high-density dislocation tangles in the martensite laths [4,22]. The prior-austenite grain size of the tested 420SS is 15.2 μm (estimated from the characteristic domain size of disorientation distance function

[4] Although the H-trapping energies of martensite block/packet boundaries have not been specifically reported [22], these martensitic boundaries could be regarded as weak H-trapping sites based on earlier simulations [29,30] and experimental results [31].

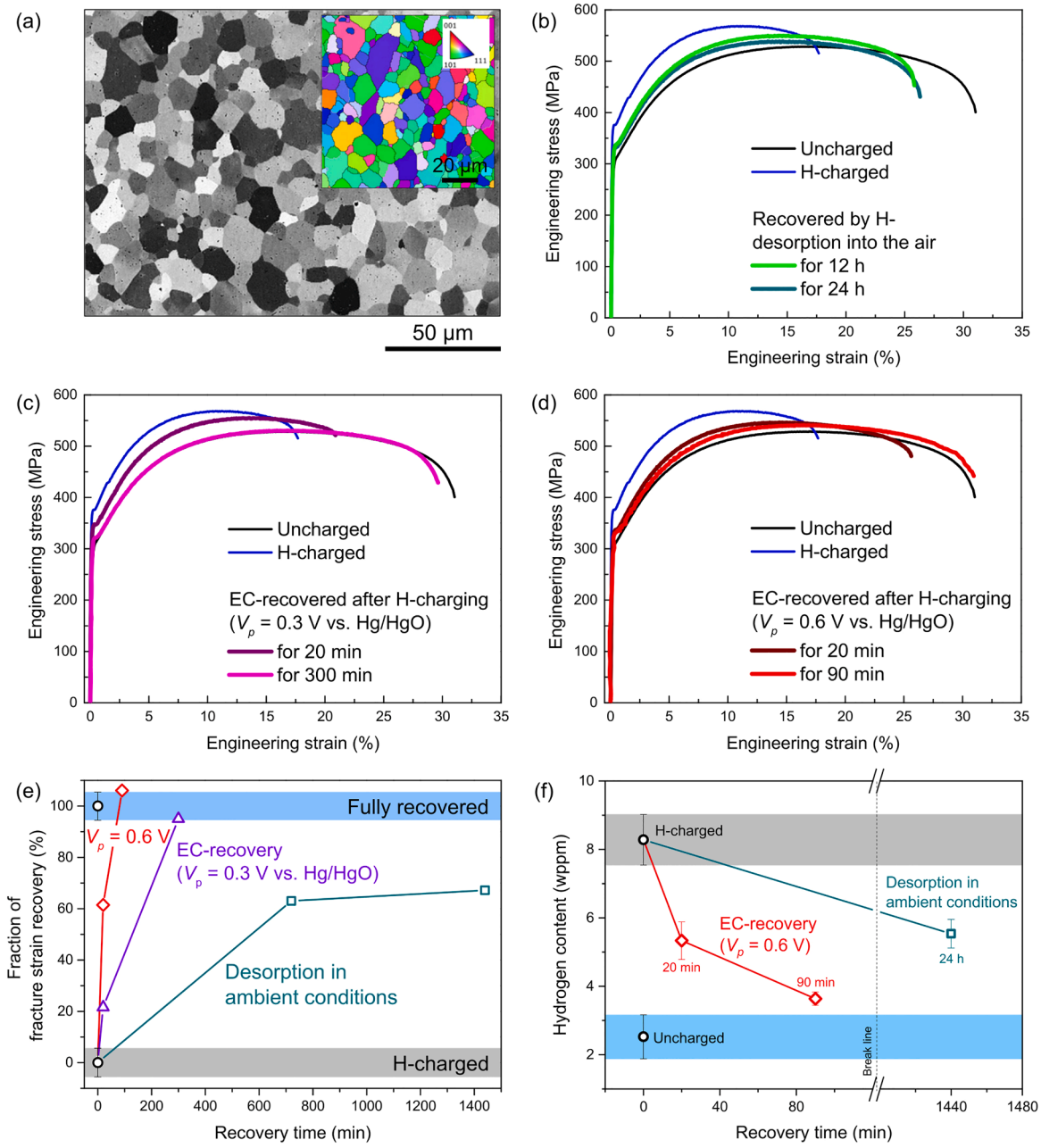

Fig. 2. (a) Back-scattered electron (BSE) image of the ferritic 430SS specimen. The inset is an inverse pole figure (IPF) map obtained from EBSD analysis. (b–d) Tensile stress-strain curves of 430SS specimens in uncharged and H-charged states, and (b) after H-desorption into the air, (c) after electrochemical (EC)-recovery with V_p = 0.3 V and (d) with V_p = 0.6 V (vs. Hg/HgO electrode). (e) Comparison of the fraction of recovery from HE among (b–d), in terms of fracture strain. (f) Comparison of the hydrogen contents in the 430SS specimens before, after H-charging, after H-desorption in the air and after EC-recovery with V_p = 0.6 V vs. Hg/HgO, respectively.

[23] using the EBSD scan). This high-strength steel with the ultimate tensile strength near 1900 MPa shows clear embrittlement behavior even after H-charging in a relatively mild condition (Condition I: i_c = 0.1 mA cm^{-2}, t = 5 min), as presented in Fig. 4(b). Although the estimated diffusion distance (L) of hydrogen in 5 min is only ~30 μm in this 420SS, the fracture strain is significantly reduced from 9.37 ± 0.18% of uncharged specimens to 4.78 ± 0.19% of H-charged specimens (averaged from 3 specimens for each case). In contrast to the ferritic 430SS, H-induced hardening is not observed in this martensitic steel. The tensile curves in Fig. 4(b) demonstrate that the electrochemically-stimulated H removal can also recover the 420SS from HE. With increasing the recovery time, the fracture strain of the specimens gradually recovers close to the pristine state. The amount of recovery by 20 min-electrochemical treatment is close to that by the uncontrolled desorption into the air for 24 h, and the material can be completely recovered from HE electrochemically in 60 min. Residual hydrogen contents in the 420SS sheets were also measured before and after H-desorption. The uncharged 420SS has 1.69 ± 0.37 wppm of H, and H-charging in condition I adds approximately 2.09 wppm of H into the specimen (total 3.78 ± 0.35 wppm H). The electrochemical treatments for 20 and 60 min reduce the H content in H-charged specimens to 3.16 ± 0.22 and 2.43 ± 0.46 wppm, respectively. This demonstrates that the degree of embrittlement in the martensitic 420SS is more sensitive to the H content compared to the case of the ferritic 430SS. Similar to the case of 430SS, ~ 0.8 wppm residue of charged H in the 420SS electrochemically treated for 60 min does not cause macroscopic embrittlement, as presented in Fig. 4(b). The

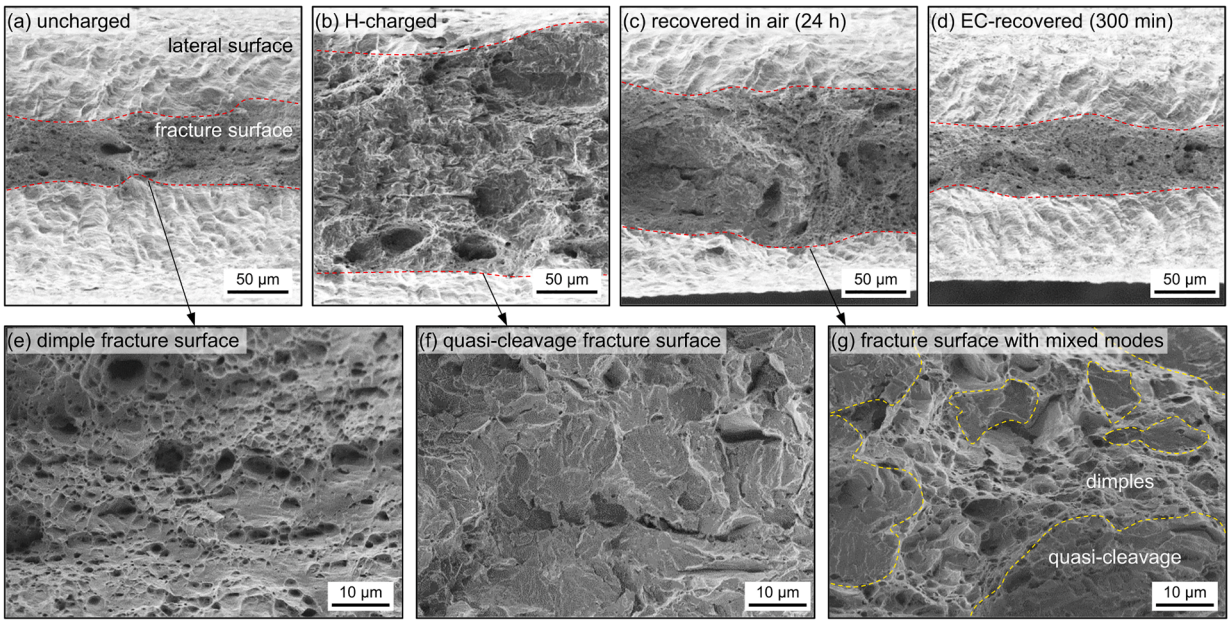

Fig. 3. Secondary electron images of fracture surfaces in 430SS specimens (a) uncharged, (b) H-charged, (c) aged in the air for 24 h, and (d) after electrochemically stimulated recovery for 300 min with $V_p = 0.3$ V. (e,f) Magnified images of (e) the uncharged specimen dominated by dimples, (f) quasi-cleavage fracture surface of the H-charged specimen, and (g) fracture surface with a mixed mode in the specimen of (c).

residual H could be mostly trapped at the carbide interface that is generally a strong H-trapping site [2]. The carbide interface acts as a preferential crack nucleation site but has only a negligible effect on crack propagation (even with H), which will be discussed later with Fig. 5.

After H-charging in a harsher condition (Condition II: $i_c = 0.5$ mA cm^{-2}, $t = 20$ min, $L \sim 61$ μm), however, the H-induced degradation of tensile properties was difficult to be recovered completely by H pumping, as shown in Fig. 4(c). The specimen after the severe H ingress fails even before reaching its original yield point, and the fracture strain averaged from 3 specimens is only 0.33 ± 0.02% in the H-charged state. Similar to the case of Condition I, the effect of 20 min-electrochemical treatment is nearly equivalent to that of the uncontrolled desorption for 24 h, but a longer electrochemical treatment (e.g. up to 60 min) was not effective for further HE recovery in this severely H-charged case. The fraction of recovery from HE in this 420SS specimen depending on H-charging conditions is summarized in Fig. 4(d). The measurement of the H contents (Fig. 5(e)) demonstrate that although a large portion of the charged H was removed by the electrochemically-stimulated desorption, the residue of charged H around 2.8 wppm still causes embrittlement of the steel. This means that, in addition to a "healable degradation" component in HE that disappears when the H is pumped out, there is an "unhealable degradation" component in HE that persists even after most of the diffusible H is pumped away. Cracks or deformation effects, which are unhealable using the proposed method, were not observed in the near-surface regions directly influenced by H-charging in the harsh condition (See Figs. S4 and S5 in Supplementary Materials). The unhealable degradation in HE of the martensitic 420SS could be attributed to the higher density of crystallographic defects in the martensitic steel, which can cause bubble-to-void transition when there is a large enough amount of trapped H at the crystallographic defects. It is known in the theory of gas-containing cavities [24,25] that at low gas chemical potential (partial pressure), there can be two different regimes of opening or cavities: a small-sized "bubble" regime that is thermodynamically stable, separated from large-sized "void" regime by a free-energy saddle point. But there can be a critical gas partial pressure, exceeding which the bubble regime loses stability (essentially merging with the "void" regime) and grows in radius in an unbounded fashion. These larger-sized voids, once formed, even if the gas partial pressure is retracted to smaller values, will not shrink, and thus can represent "unhealable degradation". In other words, once the local conditions of stress and hydrogen partial pressure cause a supercritical damage (void or crack of sufficiently large size), likely around some pre-existing interfaces, then even if the hydrogen partial pressure is reduced later, they will not heal. In extreme cases, the H bubbles can evolve into H blisters that are obvious unhealable damage incidents, as shown in an example of cold-rolled carbon steel in Supplementary Material. In contrast, the ferritic 430SS may not have reached such a critical condition, and therefore all its H-induced degradation of mechanical properties is still in the healable regime, that can disappear when the hydrogen is retracted.

We observed fractured specimens using SEM to investigate the effect of H-charging and electrochemically-stimulated healing in the damage evolution process in the martensitic steel. Series of SEM images were obtained along the polished cross-section of the fractured specimen, from the fractured edge (high local strain region) to the interior (low local strain region). The distributions of damage incidents and damage size were collected by image analysis (ImageJ [26]) from local image areas, and the damage data of each region was matched with the average local strain value of the region measured by DIC. Fig. 5(a) shows typical damage incidents observed in the specimens. Every damage incident was observed to be neighboring round carbide precipitates. All specimens analyzed exhibit the same trends that the number density of observed damages (Fig. 5(b)) increases by local strain, while the damage size does not vary significantly with increasing local strain. In other words, only the small damage incidents nucleated at the carbide-matrix interface were observed regardless of local strain level and H content in the material, and no larger cracks propagated from the damages were observed other than the major crack causing fracture. This indicates that H content does not alter the damage nucleation process but significantly reduces the resistance to crack propagation (i.e. fracture toughness), and once the micron-sized damage nucleated at the interface begins to propagate it evolves to a major crack immediately. This implies that the HE behavior of the 420SS is controlled by H trapped in the martensite microstructure (e.g. packet, block boundaries [4,22]) or possibly in the retained austenite [22,27], rather than that in the carbide interface which is known to be a strong H trapping site [2,5,22]. Overall, the results of tensile tests and damage analysis suggest that the efficiency of

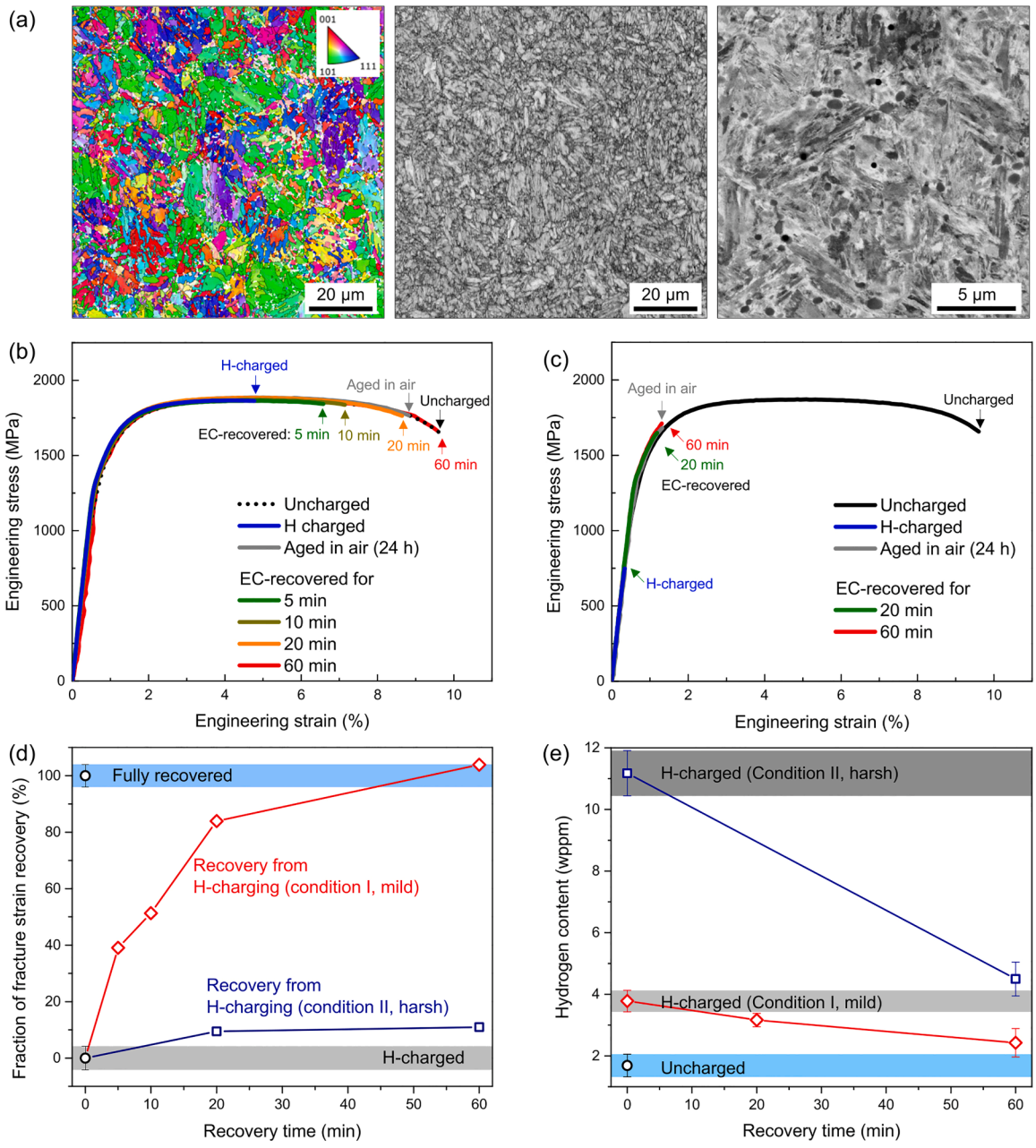

Fig. 4. (a) Microstructure images of the martensitic 420SS specimen - an IPF map (left), a band contrast image (middle) from a EBSD scan and a BSE image in a high magnification (right). The elliptical phase in a dark contrast in the BSE image is carbide precipitates. (b) Recovery of 420SS from the H-charged state of Condition I ($i_c = 0.1$ mA/cm^2, $t = 5$ min). (c) Recovery of 420SS from the H-charged state of Condition II ($i_c = 0.5$ mA/cm^2, $t = 20$ min). The H oxidation potential was 0.6 V vs. Hg/HgO for both cases of (b) and (c). (d) Comparison of the fraction of recovery from HE from the two different H-charged conditions, in terms of fracture strain. (e) Comparison of the hydrogen contents in 420SS specimens before, after H-charging in different conditions and after electrochemically stimulated recovery.

electrochemically-assisted recovery of HE depends on the types and density of H trapping sites, as well as the amount of H existing in the material.

This work demonstrates that electrochemical potential can be used to create a large driving force to desorb H from steels even at room temperature, and heal the materials from hydrogen embrittlement efficiently. The effectiveness of the electrochemically stimulated recovery is influenced by H-pumping conditions (e.g. H oxidation potential) and the type of steel, especially by H traps existing in the materials. Investigation of H trapping sites in different states after H-charging and recovery treatment using dedicated techniques such as thermal desorption spectroscopy would provide in-depth understanding of the healable and unhealable chemo-mechanical degradations by hydrogen, calling for future research.

As demonstrated in the case study of 420 SS with different charging times, the applicability of the method is also affected by the depth of trapped H (or material thickness) when it is applied to recover internal H. On the other hand, this electrochemical method of anodic polarization can be utilized to prevent unhealable HE by removing H continuously at the surface where the material is in contact with H source and blocking H ingress and accumulation within the material at source. Although this study was used in a wet environment with an aqueous electrolyte to verify the effectiveness of the methodology, the cell configuration could be modified in various ways. For example, a solid-state cell can be designed by substituting the electrolyte with a proton-conductive solid [28] or soft membrane, which would possess

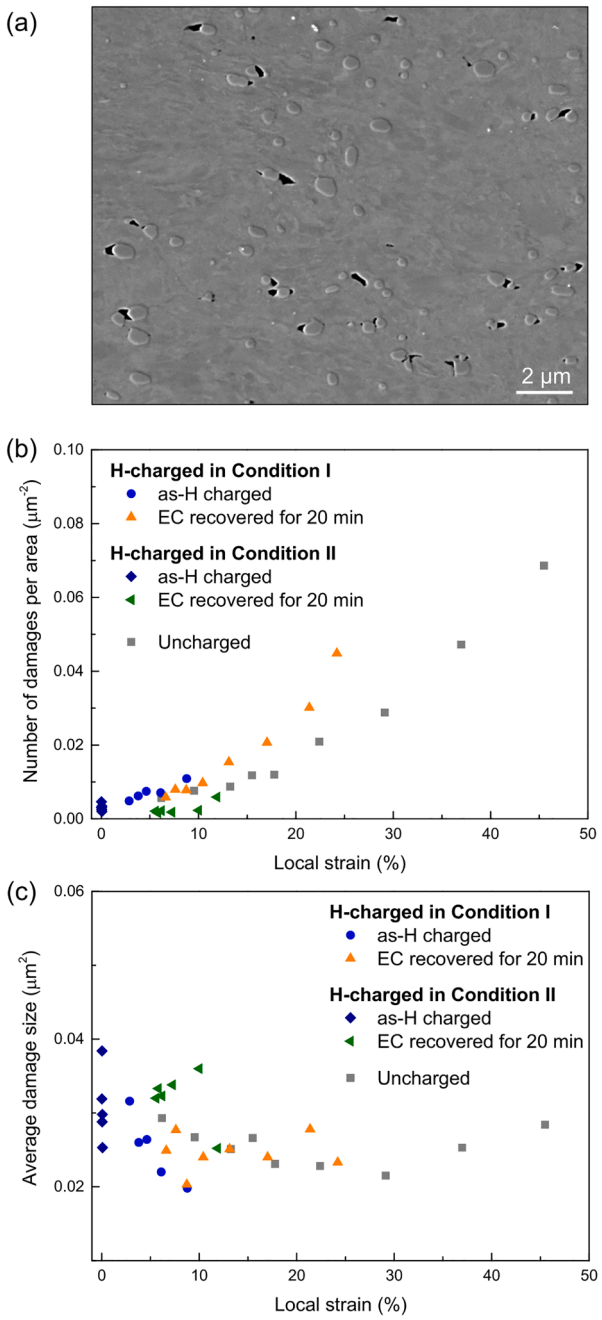

Fig. 5. (a) Secondary electron image of damages observed at the cross-section of the fractured 420SS. (b) Number density of damage incidents depending and (c) average damage size, depending on local strain in the 420SS specimens.

broader applicability to structural materials in hydrogen-rich environments.

CRediT authorship contribution statement

Jinwoo Kim: Methodology, Validation, Formal analysis, Investigation, Writing – original draft. **Xiahui Yao:** Methodology, Validation, Investigation. **Decheng Kong:** Investigation, Validation. **Ju Li:** Conceptualization, Writing – review & editing, Supervision, Funding acquisition. **Bilge Yildiz:** Conceptualization, Writing – review & editing, Supervision, Funding acquisition. **C. Cem Tasan:** Conceptualization, Writing – review & editing, Supervision, Funding acquisition.

Declaration of Competing Interest

The authors declare that they have no known competing financial interests or personal relationships that could have appeared to influence the work reported in this paper.

Data Availability

Data will be made available on request.

Acknowledgments

The authors gratefully acknowledge financial support by Exelon Corporation - Agreement Effective 4/1/16, and by U.S. Department of Energy, Office of Energy Efficiency & Renewable Energy (EERE) under Award No. DE-EE0008830.

Supplementary materials

Supplementary material associated with this article can be found, in the online version, at doi:10.1016/j.apmt.2022.101627.

References

[1] J.H. Holbrook, H.J. Cialone, E.W. Collings, E.J. Drauglis, P.M. Scott, M.E. Mayfield, Control of hydrogen embrittlement of metals by chemical inhibitors and coatings. Gaseous Hydrogen Embrittlement of Materials in Energy Technologies, Woodhead Publishing, 2012, pp. 129–153, https://doi.org/10.1533/9780857095374.1.129.
[2] H.K.D.H. Bhadeshia, Prevention of hydrogen embrittlement in steels, ISIJ Int. 56 (2016) 24–36, https://doi.org/10.2355/isijinternational.ISIJINT-2015-430.
[3] I.M. Robertson, P. Sofronis, A. Nagao, M.L. Martin, S. Wang, D.W. Gross, K. E. Nygren, Hydrogen embrittlement understood, Metall. Mater. Trans. B 46 (2015) 1085–1103, https://doi.org/10.1007/s11663-015-0325-y.
[4] J. Venezuela, Q. Liu, M. Zhang, Q. Zhou, A. Atrens, A review of hydrogen embrittlement of martensitic advanced high-strength steels, Corros. Rev. 34 (2016) 153–186, https://doi.org/10.1515/corrrev-2016-0006.
[5] T.I. Ramjaun, S.W. Ooi, R. Morana, H.K.D.H. Bhadeshia, Designing steel to resist hydrogen embrittlement: part 1–trapping capacity, Mater. Sci. Technol. 34 (2018) 1737–1746, https://doi.org/10.1080/02670836.2018.1475919 (United Kingdom).
[6] H. Luo, Z. Li, D. Raabe, Hydrogen enhances strength and ductility of an equiatomic high-entropy alloy, Sci. Rep. 7 (2017) 9892, https://doi.org/10.1038/s41598-017-10774-4.
[7] H. Luo, W. Lu, X. Fang, D. Ponge, Z. Li, D. Raabe, Beating hydrogen with its own weapon: nano-twin gradients enhance embrittlement resistance of a high-entropy alloy, Mater. Today 21 (2018) 1003–1009, https://doi.org/10.1016/J.MATTOD.2018.07.015.
[8] Y. Ogawa, H. Hosoi, K. Tsuzaki, T. Redarce, O. Takakuwa, H. Matsunaga, Hydrogen, as an alloying element, enables a greater strength-ductility balance in an Fe-Cr-Ni-based, stable austenitic stainless steel, Acta Mater. 199 (2020) 181–192, https://doi.org/10.1016/j.actamat.2020.08.024.
[9] A.T. Paxton, A.P. Sutton, M.W. Finnis, The challenges of hydrogen and metals, Philos. Trans. R. Soc. A Math. Phys. Eng. Sci. 375 (2017), 20170198, https://doi.org/10.1098/rsta.2017.0198.
[10] H. Barthelemy, M. Weber, F. Barbier, Hydrogen storage: recent improvements and industrial perspectives, Int. J. Hydrog. Energy 42 (2017) 7254–7262, https://doi.org/10.1016/J.IJHYDENE.2016.03.178.
[11] H. Dogan, D. Li, J.R. Scully, Controlling hydrogen embrittlement in precharged ultrahigh-strength steels, Corrosion 63 (2007) 689–703, https://doi.org/10.5006/1.3278418.
[12] M.J. Robinson, R.M. Sharp, Effect of post-exposure heat treatment on the hydrogen embrittlement of high carbon steel, Corrosion 41 (1985) 582–586, https://doi.org/10.5006/1.3582987.
[13] K. Verbeken, Analysing hydrogen in metals: bulk thermal desorption spectroscopy (TDS) methods. Gaseous Hydrogen Embrittlement of Materials in Energy Technologies, Woodhead Publishing, 2012, pp. 27–55, https://doi.org/10.1533/9780857095374.1.27.
[14] ASTM Standard G148-97, Standard Practice for Evaluation of Hydrogen Uptake, Permeation, and Transport in Metals by an Electrochemical Technique, ASTM International, West Conshohocken, PA, USA, 2018, https://doi.org/10.1520/G0148-97R18.
[15] C. San Marchi, J.A. Zelinski, High-alloy ferritic steels: Ferritic stainless steels (code 1500). in: C. San Marchi, B.P. Somerday, Technical reference on hydrogen compatibility of materials, SAND2008-1163, Sandia National Laboratories, Livermore, CA, USA, 2008. https://www.sandia.gov/matlsTechRef/.
[16] M. Koyama, D. Yamasaki, T. Nagashima, C.C. Tasan, K. Tsuzaki, *In situ* observations of silver-decoration evolution under hydrogen permeation: effects of

grain boundary misorientation on hydrogen flux in pure iron, Scr. Mater. 129 (2017) 48–51, https://doi.org/10.1016/J.SCRIPTAMAT.2016.10.027.
[17] Y.S. Chen, H. Lu, J. Liang, A. Rosenthal, H. Liu, G. Sneddon, I. Mccarroll, Z. Zhao, W. Li, A. Guo, J.M. Cairney, Observation of hydrogen trapping at dislocations, grain boundaries, and precipitates, Science 175 (2020) 171–175.
[18] Y.S Chen, D. Haley, S.S.A Gerstl, A.J. London, F. Sweeney, R.A. Wepf, W. M. Rainforth, P.A.J. Bagot, M.P. Moody, Direct observation of individual hydrogen atoms at trapping sites in a ferritic steel, Science 355 (2017) 1196–1199, https://doi.org/10.1126/science.aal2418.
[19] A.J. Kumnick, H.H. Johnson, Deep trapping states for hydrogen in deformed iron, Acta Metall. 28 (1980) 33–39.
[20] A.A. Pisarev, Hydrogen adsorption on the surface of metals. Gaseous Hydrogen Embrittlement of Materials in Energy Technologies, Woodhead Publishing, 2012, pp. 3–26, https://doi.org/10.1533/9780857095374.1.3.
[21] C.W. San Marchi, J.A. Ronevich. Austenitic stainless steel research at Sandia national laboratories and H-Mat consortium, SAND2019-14323PE, Sandia National Laboratories, Livermore, CA, USA, 2019.
[22] F.G. Wei, K. Tsuzaki, Hydrogen trapping phenomena in martensitic steels. Gaseous Hydrogen Embrittlement of Materials in Energy Technologies, Woodhead Publishing, 2012, pp. 493–525, https://doi.org/10.1533/9780857093899.3.493.
[23] L. Morales-Rivas, V.A. Yardley, C. Capdevila, C. Garcia-Mateo, H. Roelofs, F. G. Caballero, A procedure for indirect and automatic measurement of prior austenite grain size in bainite/martensite microstructures, J. Mater. Sci. 50 (2015) 258–267, https://doi.org/10.1007/s10853-014-8584-6.
[24] K.C. Russell, Thermodynamics of gas-containing voids in metals, Acta Metall. 20 (1972) 899–907. https://www.sciencedirect.com/science/article/pii/0001616072900831.
[25] G.R. Odette, M.J. Alinger, B.D. Wirth, Recent developments in irradiation-resistant steels, Annu. Rev. Mater. Res. 38 (2008) 471–503, https://doi.org/10.1146/annurev.matsci.38.060407.130315.
[26] W.S. Rasband, ImageJ, U.S. National Institutes of Health, Bethesda, MD, USA, 1997-2018. https://imagej.nih.gov/ij/.
[27] M. Enomoto, D. Hirakami, T. Tarui, Thermal desorption analysis of hydrogen in high strength martensitic steels, Metall. Mater. Trans. A 43 (2012) 572–581, https://doi.org/10.1007/s11661-011-0909-3.
[28] S. Wang, H. Jiang, Y. Dong, D. Clarkson, H. Zhu, C.M. Settens, Y. Ren, T. Nguyen, F. Han, W. Fan, S.Y. Kim, J. Zhang, W. Xue, S.K. Sandstrom, G. Xu, E. Tekoglu, M. Li, S. Deng, Q. Liu, S.G. Greenbaum, X. Ji, T. Gao, J. Li, Acid-in-clay electrolyte for wide-temperature-range and long-cycle proton batteries, Adv. Mater. 34 (2022), 2202063, https://doi.org/10.1002/adma.202202063.
[29] E.J. McEniry, T. Hickel, J. Neugebauer, Hydrogen behaviour at twist {110} grain boundaries in α-Fe, Philos. Trans. R. Soc. A Math. Phys. Eng. Sci. 375 (2017), 20160402, https://doi.org/10.1098/rsta.2016.0402.
[30] J. Li, A. Hallil, A. Metsue, A. Oudriss, J. Bouhattate, X. Feaugas, Antagonist effects of grain boundaries between the trapping process and the fast diffusion path in nickel bicrystals, Sci. Rep. 11 (2021) 15533, https://doi.org/10.1038/s41598-021-94107-6.
[31] T. Nagashima, M. Koyama, A. Bashir, M. Rohwerder, C.C. Tasan, E. Akiyama, D. Raabe, K. Tsuzaki, Interfacial hydrogen localization in austenite/martensite dual-phase steel visualized through optimized silver decoration and scanning Kelvin probe force microscopy, Mater. Corros. 68 (2017) 306–310, https://doi.org/10.1002/maco.201609104.